Supplementary Information

Microwave-assisted synthesis of polyoxometalate-Dy_2O_3 monolayer nanosheets and nanotubes

Maria C. Dipalo[1], Biao Yu[1], Xijun Cheng[1], Siyang Nie[1], Junli Liu[1], Wenxiong Shi[2], Fenghua Zhang[1]*, Qingda Liu[1]*, Xun Wang[1]*

[1]Engineering Research Center of Advanced Rare Earth Materials, Department of Chemistry, Tsinghua University, Beijing 100084, China

[2]Institute for New Energy Materials and Low Carbon Technologies, School of Materials Science and Engineering, Tianjin University of Technology, Tianjin 300387, China

E-mail: wangxun@mail.tsinghua.edu.cn

Table of Contents

1. Supplementary Methods

Materials

The reagents used are oleylamine (OAM) (J&K Scientific LTD) for a quantity always equal to 2.7 mL; Oleic Acid (OA), phosphomolybdic acid hydrate (PMA), linoleic acid (LA) (Sinopharm Chemical Reagent Beijing Co., Ltd.); H_2O deionized; $DyCl_3 \cdot 6H_2O$ (Innochem Technology Co. LTD); n-Octylamine (n-O) (Aladdin Industrial Corporation); phosphotungstic acid hydrate (PWA) (Alfa Aesar Co., Ltd). The nanoparticles were then washed three times with ethanol and cyclohexane (Sinopharm Chemical Reagent Co., Ltd). All chemicals were used as received without further purification. **Characterization**

Inductively coupled plasma atomic emission spectroscopy ICP-OES was carried out on iCAP 6300 ThermoFisher. TEM photos were made with a Hitachi H-7700 at 100 KV. High-resolution transmission electron microscopy (HR-TEM), high angle annular dark field scanning transmission electron microscopy (HAADF-STEM), and Energy Dispersive X-Ray (EDX) spectroscopy were characterized at 200 KV by a Tecnai G2 F20 S-Twin microscope. XRD patterns were obtained with a Bruker D8 Advance X-Ray diffractometer using Cu Kα radiation (λ=1.5418 Å). Small-angle X-ray diffraction (SAXRD) was tested on a Rigaku D/max-2500/PC X-ray diffractometer, and Cu Kα radiation (λ=1.5418 Å). Fourier transform infrared FT-IR was obtained with a Perkin Elmer Spectrum. Thermogravimetric analysis (TGA) was performed with NETZSCH STA449F3. Electrospray ionization mass spectrometry (ESI-MS). X-ray photoelectron spectroscopy (XPS) was obtained by a scanning X-ray microprobe (Quantera SXM, ULVAC-PHI. INC) at 250 kV, 55 eV with monochromatic Al Kα radiation. Microwave synthesis was performed with Biotage Initiator with a power range of 0-300 W at 2.45 GHz.

Method

After the reaction in the microwave, at 165 degrees. The cap of the sealed vial was removed, and the dry gelatinous part above the solution was mechanically removed and thrown away, the liquid below was washed with cyclohexane and ethanol three times and centrifuged each time at 9000 rpm. Subsequently, it was dispersed in 1mL of cyclohexane and one drop of this compound was diluted in

1 additional mL of cyclohexane, and 3 drops were applied on a TEM plate.

The product comes out of the microwave at 50 degrees centigrade. When it reaches room temperature, everything tends to solidify as a gel. Making it impossible to distinguish where the nanowires are contained and where the nanosheets are. This means that to extract it is necessary to insert cyclohexene and ethanol in the glass vial. Going, therefore, to bring everything into solution. It has been seen that even for centrifuges between 9000-8000 rpm, it is impossible to separate the 1D from the 2D structures. For this it's important when still hot, to work the sample. The gelatinous part that was deposited along the walls of the glass vial was thrown because it was rich in 1D nanowires, probably created in the initial stage of the reaction, when the pressure grew to 8 bar, and then quickly dropped to 1 bar. It is easy to think that these nanowires are created at first, then aggregated in a short time like a net, if in solution with oleic acid, thanks also to the heat generated by the microwaves to form the nanosheets.

This problem of excess nanowires was found in the use of the oven but in smaller quantities. Probably because the aggregation process is slower, and therefore also the pressure rises less.

The pressure limit for the nanosheet is 8 bar, and for the nanotube is 5 bar.

The yield obtains of Dy_2O_3-PMA heterostructures based on microwave synthesis is 64%.

2. Molecular Dynamics Simulation

Models

The charge of metal oxide was obtained by quantum calculation.[1], [2], [3] The model for PMo_{12}, metal oxide, and protonated oleylamine can be obtained from reference and our former work.[4], [5], [6], [7] The GROMACS and the GROMOS96 force fields were used in the MD simulations.[8], [9], [10], [11], [12]

Simulations of nanosheet assembly

To study the formation of Sub- nanosheet, the PMo_{12} were placed in a $12\times10.392\times12$ nm^3 simulation box, pre-aligned as a hexagonal pattern with the amount of 100. The 325 Dy_2O_3 and 300 protonated oleylamine molecules were put into the vacuum box around the PMo_{12} randomly. The amounts of Dy_2O_3 and protonated oleylamine were obtained from experimental results. The positions of these PMo_{12} were frozen and other molecules can move freely during the simulation. The cutoff distance for short-range non-bonded interactions was chosen to be 12 Å and long-range electrostatic and V-rescale bath coupling schemes were used. [13], [14] The NVT Ensemble was applied, and the simulations were run over 4000 ps in steps of 2 fs. The figures of simulation results were captured by VMD.[15]

Simulations of nanotube assembly

To study the formation of the nanotube, 240 PMo_{12} were placed in a simulation box, pre-aligned as a tube with a hexagonal pattern with a dimension size of $20\times 20\times 10.39$ nm^3. The amounts of Dy_2O_3 (800) and protonated oleylamine (720) were inserted into the simulation box with the ratio obtained from experimental results. The diameter of the tube is about 12 nm. The positions of these POMs were frozen and other molecules could move freely during the simulation. The NVT ensemble was applied, and the simulations were run over 4000 ps in steps of 2 fs. Other simulation details are similar to those described above.

3. Density Functional Theory Study

All spin-polarized density functional theory (DFT) calculations were performed by using the Vienna ab initio simulation package (VASP) with plane-wave pseudopotential. [16], [17] The cutoff of kinetic energy was 450 eV. The generalized gradient approximation (GGA) in the Perdew-Burke-Ernzerh of (PBE) functional was used to describe exchange and correlation energies.[18] The projector-augmented wave (PAW) method was used to represent the core-valence interaction. [19], [20], [21]The Brillouin zone was sampled with a 1 × 1 × 1 k-points grid based on the Monkhorst-Pack scheme. To accurately treat the highly localized 3d orbitals of Ni, spin-polarized DFT+U calculations were considered with a value of U_{eff} = 4.0. [22], [23] The atomic positions were relaxed until the force on each atom was less than 0.01 eV/Å and electronic energies were converged within 10^{-4} eV.

The initial structure was built according to the ICP-AES results and based on our previous works. [24] The model has a vacuum of 15 Å along the Z-axis, which was large enough to avoid interaction between the slabs obtained after replication in the three space dimensions. During the optimization of the initial slab, all the positions of atoms, and length of axes, and the shape of the box could not be restricted, except for the Z-axis.

POM clusters possess the ability to partake in the growth processes of nanostructures, exhibiting vastly different assembly behaviors compared to their inorganic counterparts such as metal oxide/sulfide. [25] With a fixed size akin to nuclei, POM clusters primarily assemble with said nuclei through noncovalent interactions, thereby altering conventional growth pathways and resulting in subnanometer structures with smaller critical sizes. [26], [27] In our previous study, we employed experimental techniques including atomic-resolution HAADF-STEM [28] and cryo-electron microscopy [29] to investigate the arrangement pattern between POM and inorganic nuclei in subnanomaterials synthesized via the cluster-nuclei coassembly strategy. Our findings revealed a periodically repeated "A-B-A-B" structure of POM and inorganic nuclei. Classical molecular dynamics simulations suggested that inorganic nuclei can exist stably around POM clusters. Additionally, our previous work using ab initio molecular dynamics under 410 K demonstrated that POM can capture MnO nuclei and facilitate the formation of long-ranged "A-B-A-B" (A stands for DyO and B represents POM) structures.[30]

4. Optoelectronic Experimental

We studied the photoresponse in a three-electrode system (Shanghai Chenhua CH1660E) with the first electrode having an ITO-coated glass (photoanode), the second a platinum electrode (photocathode) and the third an Ag/AgCl reference electrode. And a PEC-type photodetection system (PEC 2000, photoelectrochemical test system, Beijing Perfectlight Technology Co., Ltd). An aqueous solution of Dipotassium hydrogen phosphate trihydrate ($K_2HPO_4 \cdot 3H_2O$) and Potassium dihydrogen phosphate (KH_2PO_4) was used. For the light source, a Xenon lamp (Beijing Perfect Light Technology Co., Ltd.) The spectral range of the Xenon lamp is 320~780 nm and the power density of light is 200 mW cm^{-2}. The transient photocurrent response was measured by manually switching the Xenon lamp on and off every 20 s. [31]

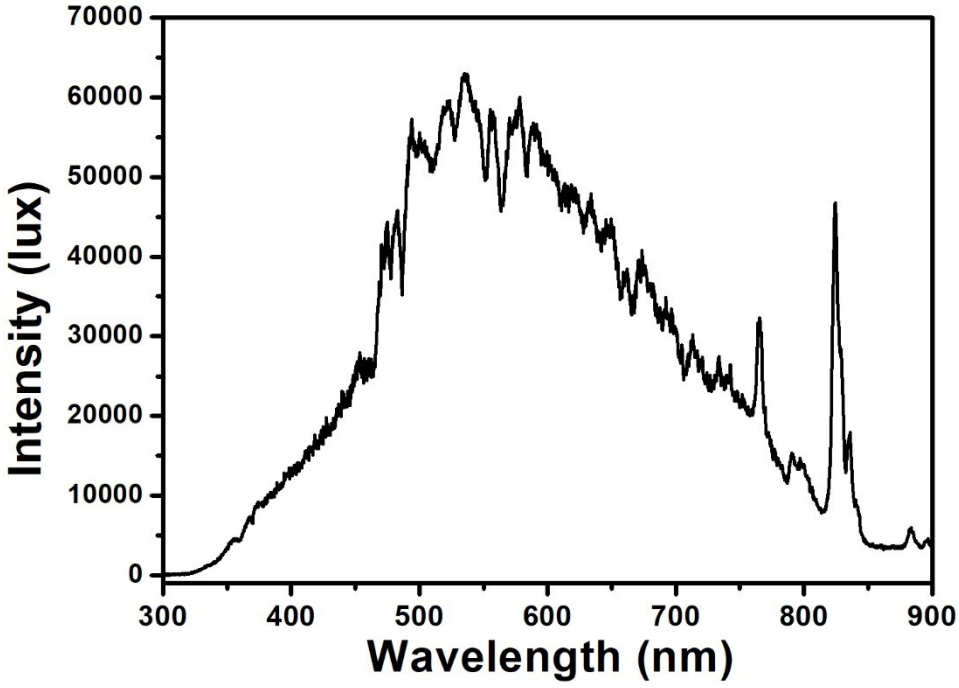

Fig. S1 Spectrum and intensity of the Xenon light source.

5. Supplementary Figures and Tables

Tab. S1 Reaction a (Dy-PMA-1), reaction b (Dy-PMA-2), reaction c (Dy-PMA-3), reaction d (Dy-PMA-4), reaction e (Dy-PMA-5), reaction f (Dy-PMA-6)

Reaction	Time (hour)	Temp. (°C)	POM (Mo)	POM (W)	Dy (g)	H_2O (mL)	OAM (mL)	OA (mL)	n-Octyl. (mL)	Lin. Ac. (mL)
Dy-PMA-1	2	165	0.05	0	0.04	0.22	2.7	0.5	0	0
Dy-PMA-2	4	165	0.05	0	0.06	0.22	2.7	0.34	0	0
Dy-PMA-3	6	165	0.05	0	0.06	0.22	2.7	0.34	0	0
Dy-PMA-4	2	165	0.05	0	0.06	0.22	0	0	2.7	0.75
Dy-PMA-5	2	165	0	0.03	0.06	0.22	2.7	0.9	0	0
Dy-PMA-6	2	165	0	0.03	0.06	0.22	2.7	0.7	0	0

Tab. S2 ICP-OES data of Dy_2O_3-PMA SNSs and NTs

	Weight %			Atomic ratio %		
	Dy-PMA-1	**Dy-PMA-2**	**Dy-PMA-3**	**Dy-PMA-1**	**Dy-PMA-2**	**Dy-PMA-3**
Mo	23.2	24.7	24.5	0.242	0.257	0.255
P	0.546	0.142	0.345	0.018	0.005	0.011
Dy	21.2	22.7	26.6	0.13	0.14	0.164

Supplementary Figures

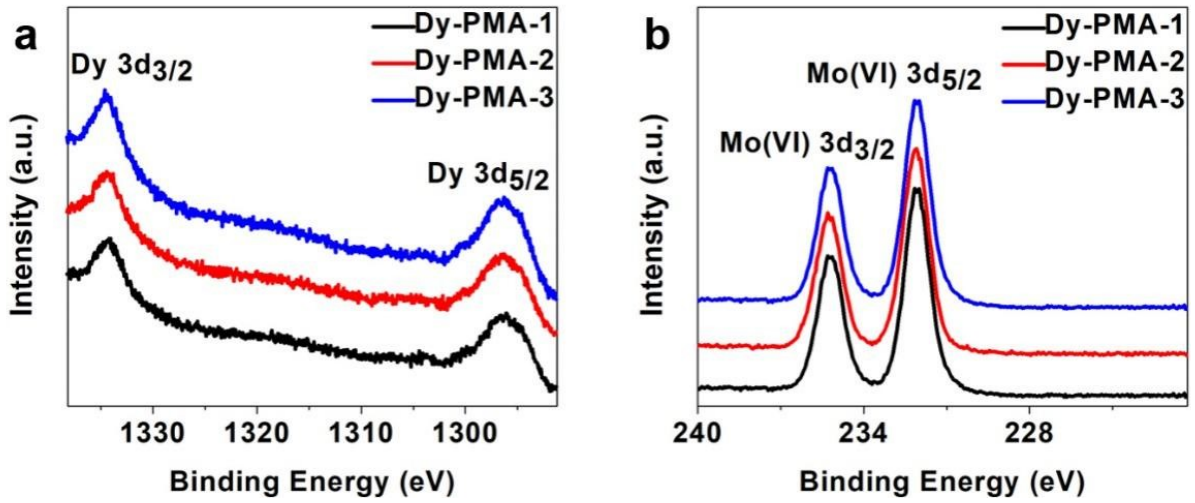

Fig. S2 XPS spectrums of (a) Dy 3d and (b) Mo^{6+} 3d in Dy_2O_3-PMA SNSs and NTs.

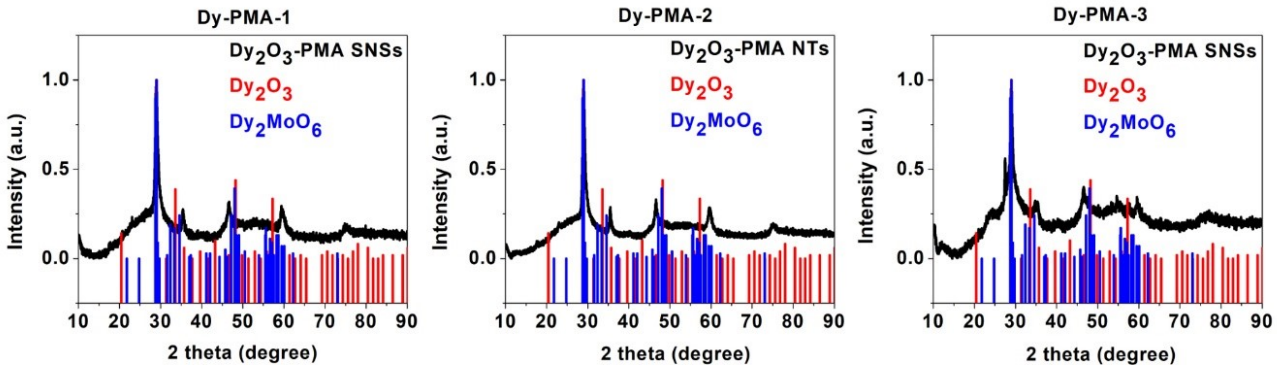

Fig. S3 XRD spectrums

Tab. S3 Reactions in **Fig. S4**.

React. No	Time (hour)	Temp. (°C)	$DyCl_3$ (g)	H_2O (mL)	OAM (mL)	OA (mL)	n-Octil. (mL)	Lin. Ac. (mL)
a	2	165	0.04	0.22	2.7	0.5		
b	4	165	0.06	0.22	2.7	0.34		
c	12 Oven	165	0.06	0.22	2.7	0.34		
d	2	165	0.06	0.22			2.7	0.75
e	2	165	0.06	0.22	2.7	0.9		
f	2	165	0.06	0.22	2.7	0.7		

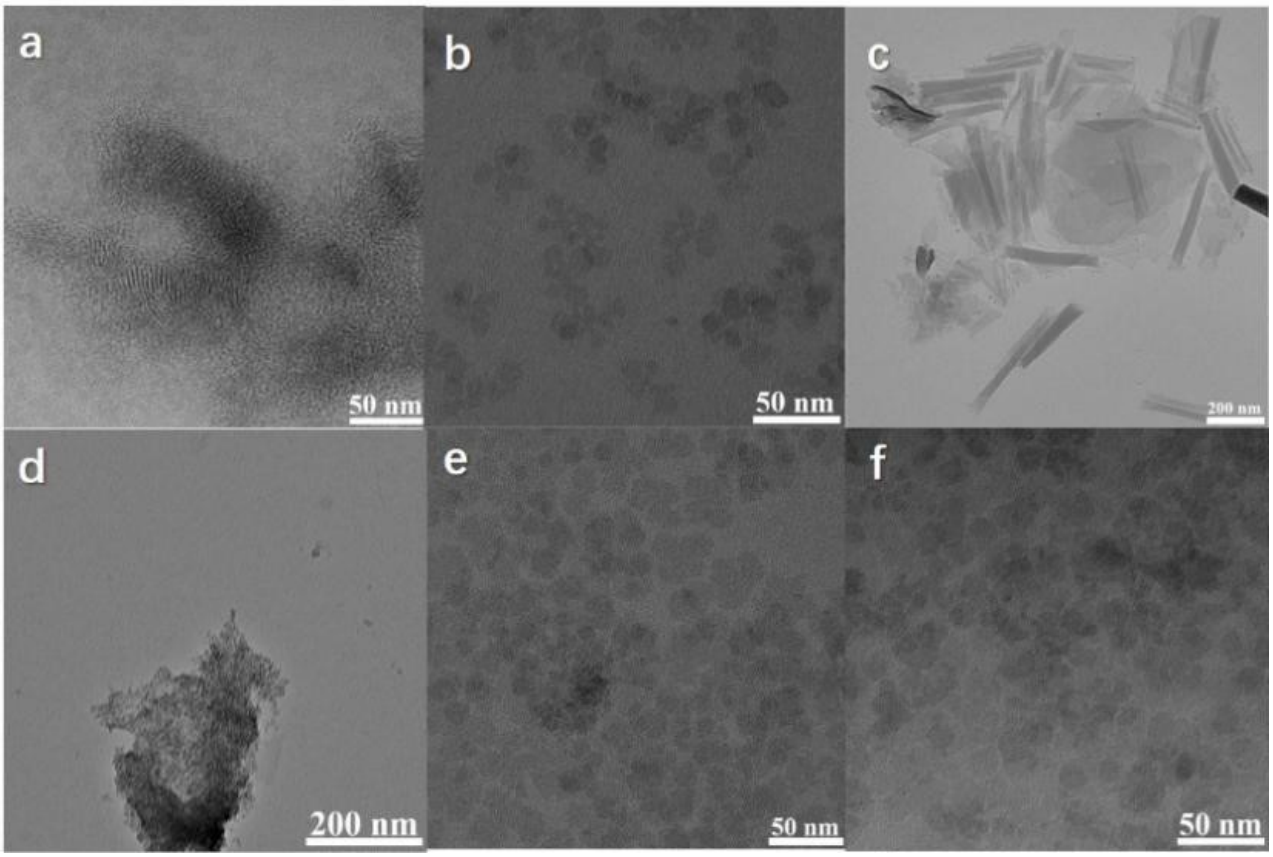

Fig. S4 Reactions in the absence of PMA, (a) and (d) do not show nanoparticles; (b), (f), and (e) show non-well-defined and homogeneous nanoparticles; (c) the reaction in the Oven in the absence of POM, shows some nanorods mixed with nanosheets and other impurities.

Tab. S4 Reactions in **Fig. S5**.

React. Dy-PMA-1	Time	Temp. (°C)	PMA (g)	$DyCl_3$ (g)	H_2O (mL)	OAM (mL)	OA (mL)
a	2 h	165	0.05	0.04	0.22	2.7	0.5
b	0 h	165	0.05	0.04	0.22	2.7	0.5
c	30 s	165	0.05	0.04	0.22	2.7	0.5
d	1 min	165	0.05	0.04	0.22	2.7	0.5
e	5 min	165	0.05	0.04	0.22	2.7	0.5
f	30 min	165	0.05	0.04	0.22	2.7	0.5
g	1 h	165	0.05	0.04	0.22	2.7	0.5

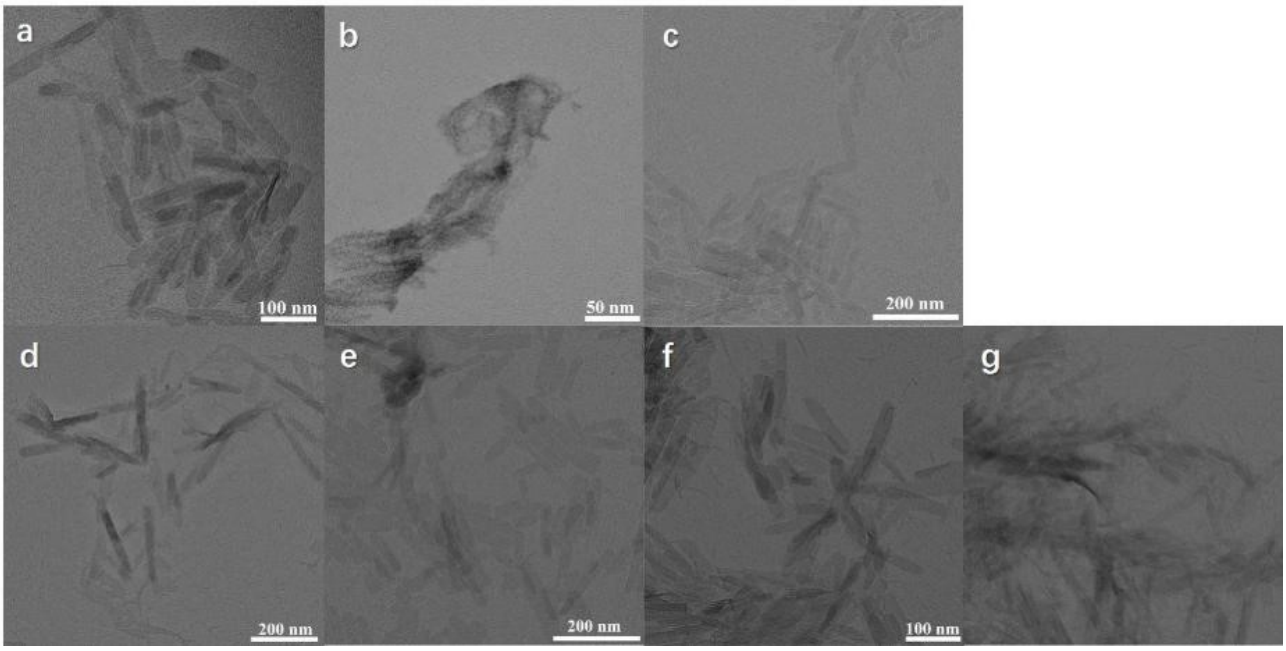

Fig. S5 Reactions at different reaction times Dy-PMA-1. (a) reaction studied at 2h at 165 degrees centigrade; (b) reaction at zero-time; (c) reaction time 30 seconds; (d) reaction time 1 min; (e) reaction time 5 min; (f) reaction time 30 min; (g) reaction time 1 h.

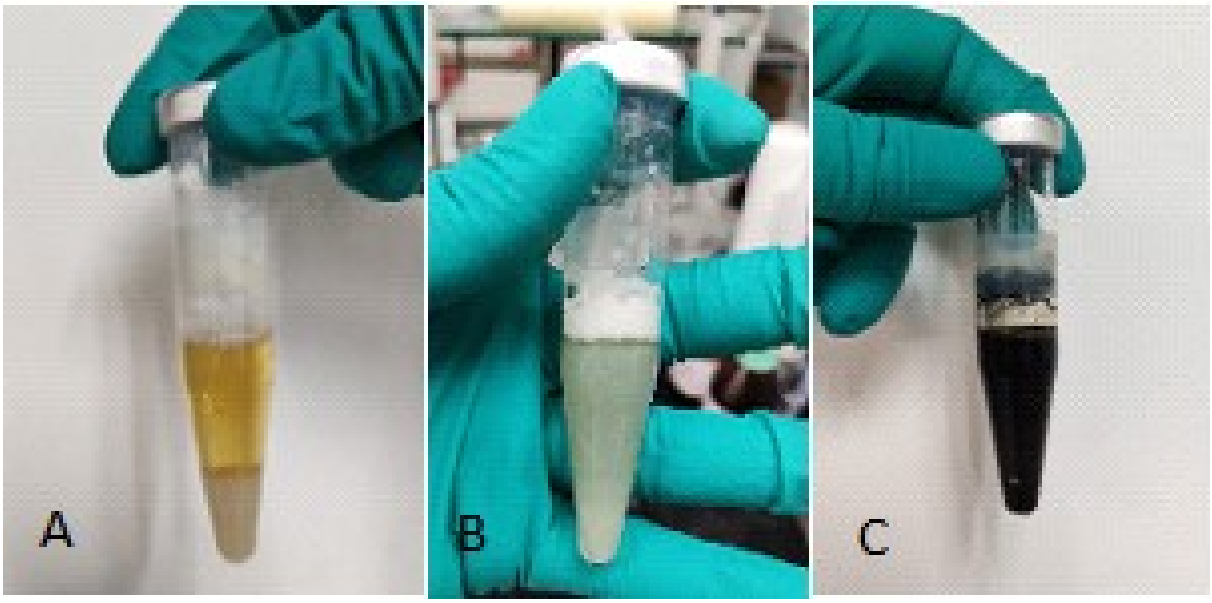

Fig. S6 (A) Reaction C; (B) Reaction E; (C) Reaction F.

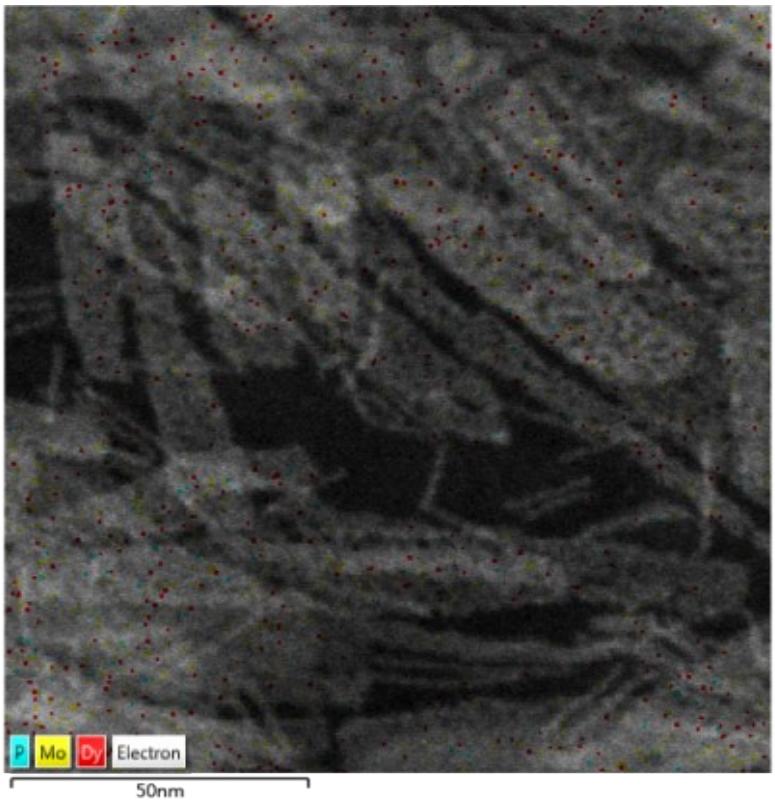

Fig. S7 Shows the presence even at 30 seconds of Dy and POM inside the nanoparticles.

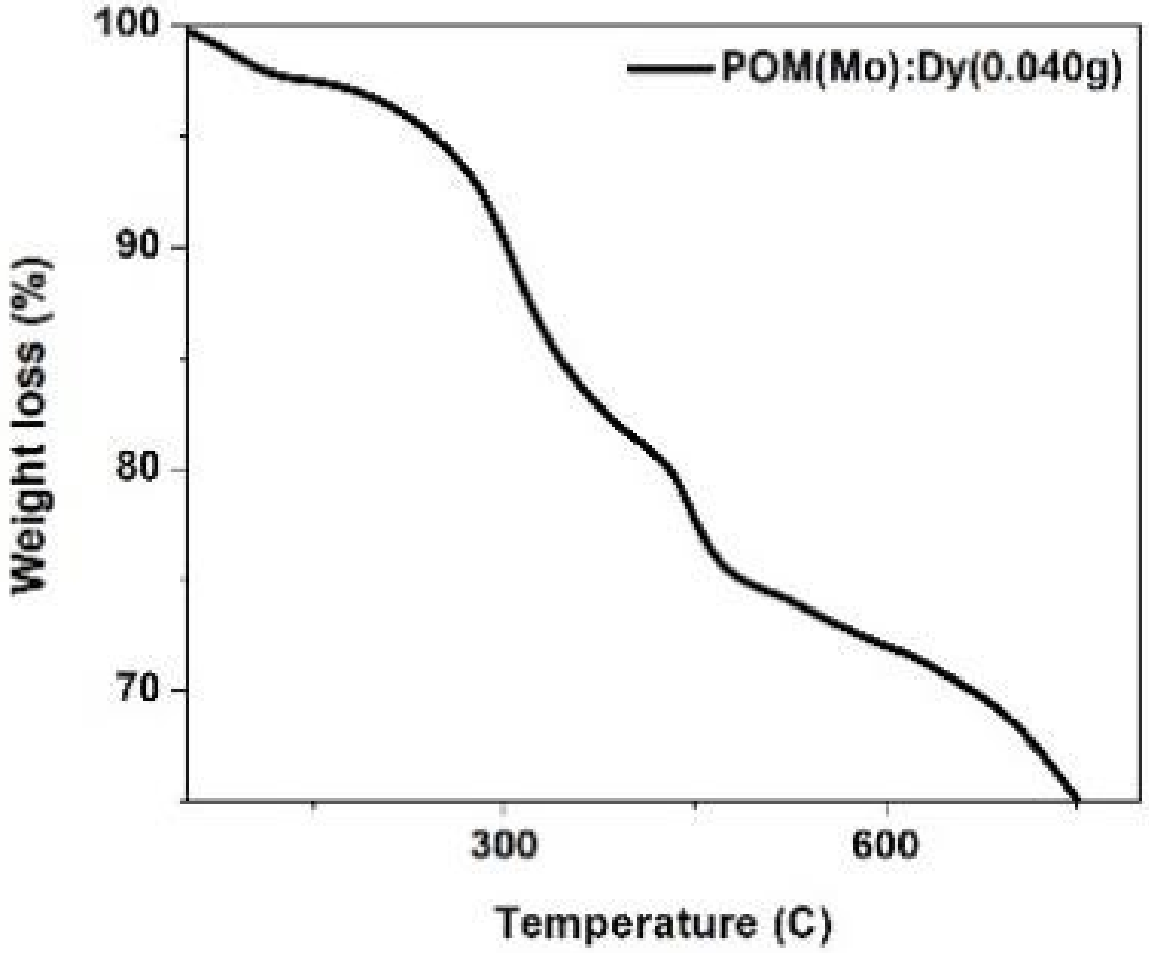

Fig. S8 Weight loss of 24% given from the decomposition of the organic components of oleylamine and oleic acid between 200-450 ˚C and one loss of inorganic components above 450 ˚C, with an initial loss of 3% till 100 ˚C of H_2O for a total loss of 27%.

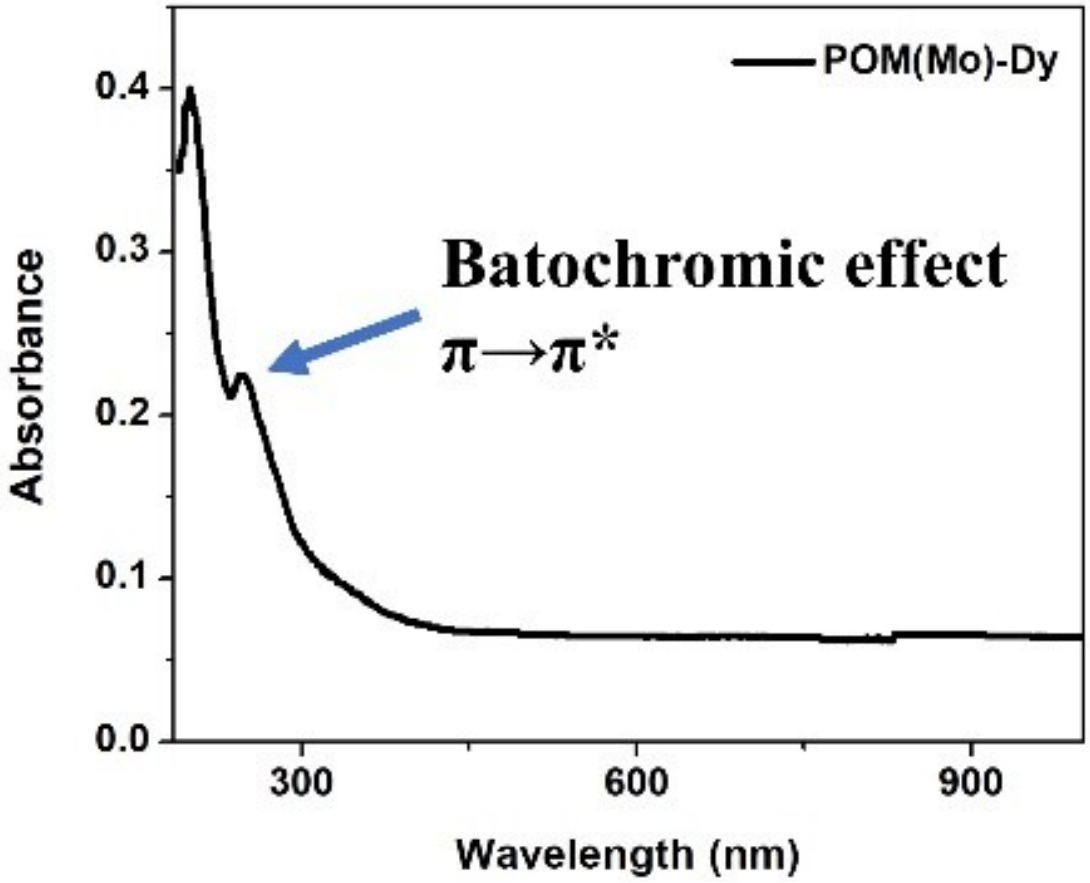

Fig. S9 Bis Dy-PMA-1 in UV-vis spectra, show a Batochromic effect $\pi \rightarrow \pi^*$ correlated probably with the resonance of the PMA Molibdenum.

Tab. S5 Reactions in **Fig. S10**

React. Dy-PMA-2	Time	Temp. (°C)	POM (Mo)	POM (W)	Dy (g)	H_2O (mL)	OAM (mL)	OA (mL)
a	4 h	165	0.05		0.06	0.22	2.7	0.34
b	0 h	165	0.05		0.06	0.22	2.7	0.34
c	1 min	165	0.05		0.06	0.22	2.7	0.34
d	5 min	165	0.05		0.06	0.22	2.7	0.34
e	30 min	165	0.05		0.06	0.22	2.7	0.34
f	1 h	165	0.05		0.06	0.22	2.7	0.34
g	6 h	165	0.05		0.06	0.22	2.7	0.34

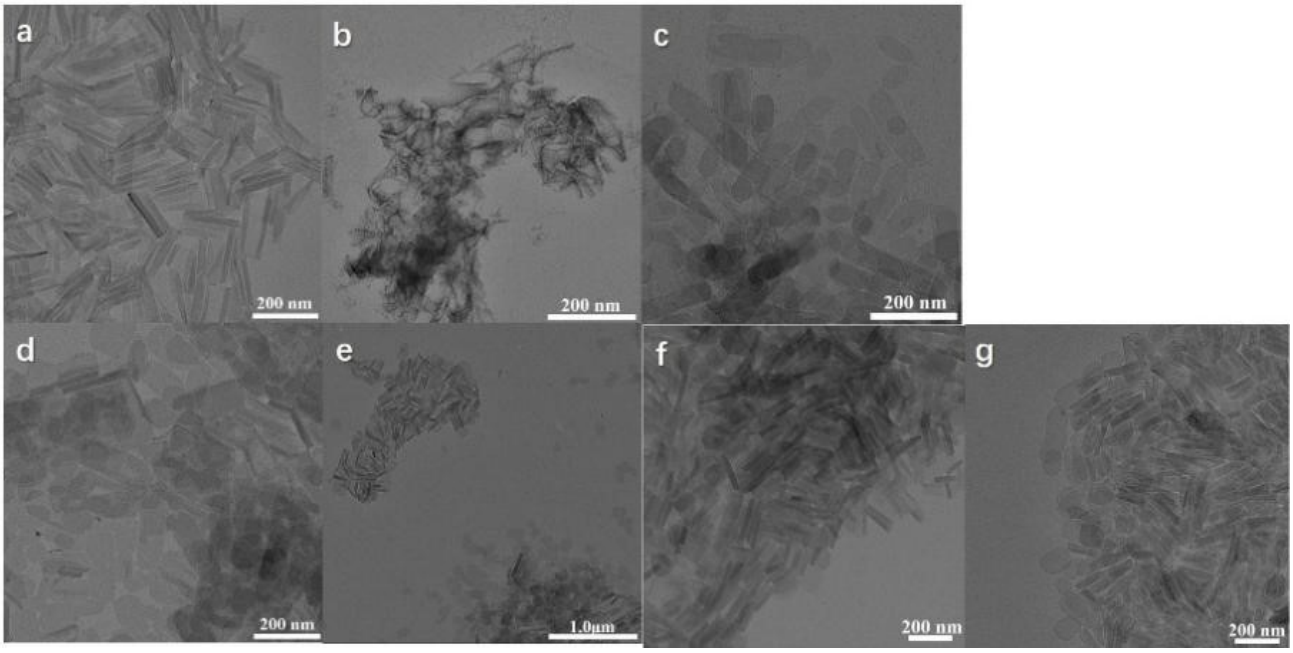

Fig. S10 Reactions at different reaction times Dy-PMA-2. (A) reaction studied at 4h at 165 degrees centigrade; (B) reaction at zero-time; (C) reaction time 1 min; (D) reaction time 5 min; (E) reaction time 30 min; (F) reaction time 1 h; (G) reaction time 6 h.

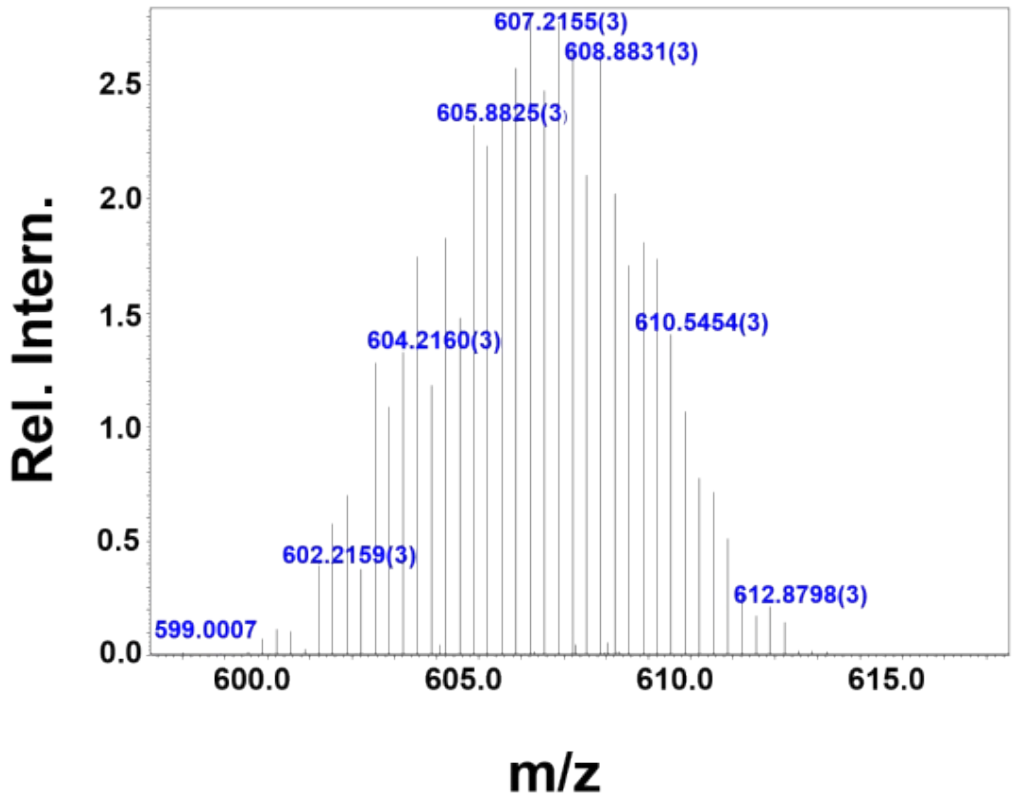

Fig. S11 Presence of POM.

Tab. S6 Reactions in **Fig. S12**

React.	Time (hour)	Temp. (°C)	POM (Mo)	Dy (g)	H_2O (mL)	OAM (mL)	OA (mL)
a	4	80	0.05	0.06	0.22	2.7	0.34
b	4	120	0.05	0.06	0.22	2.7	0.34
c	4	165	0.05	0.06	0.22	2.7	0.34
d	4	180	0.05	0.06	0.22	2.7	0.34

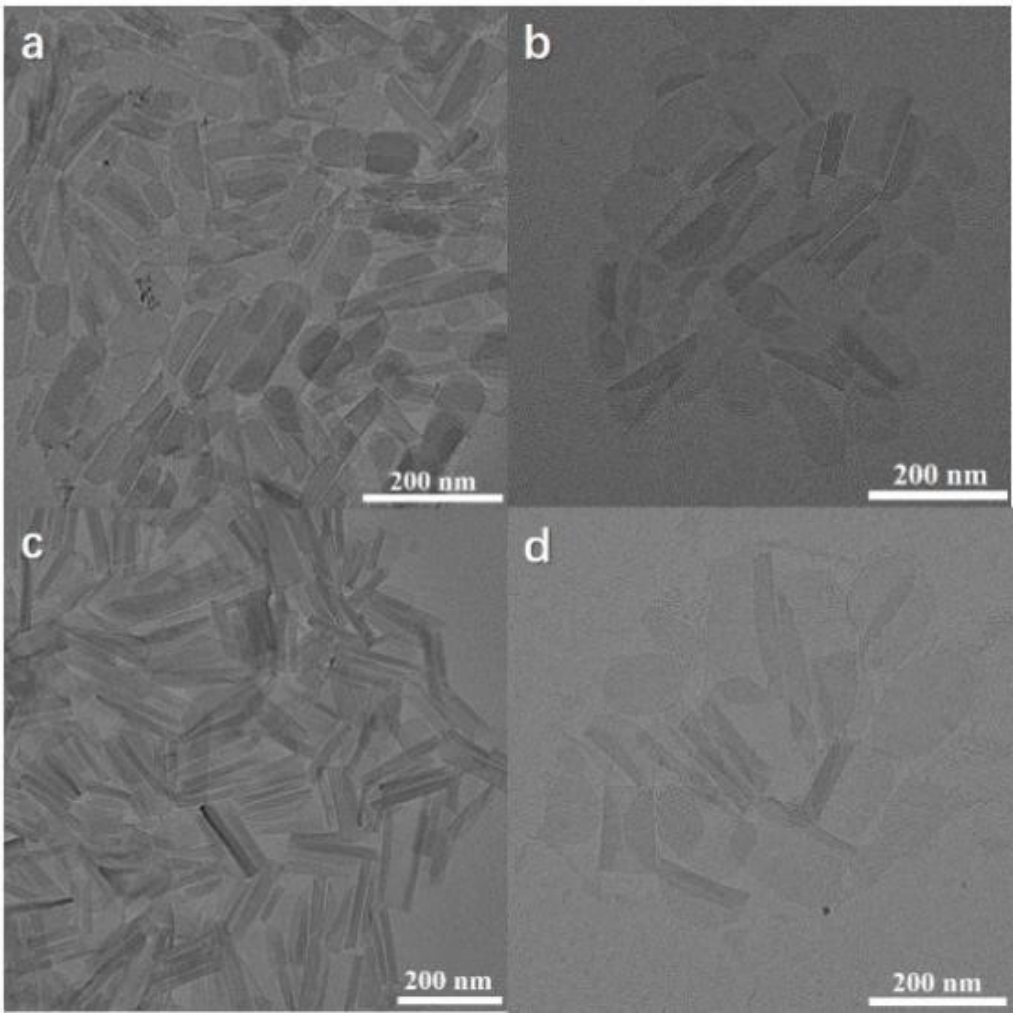

Fig. S12 Reactions at different temperatures Dy-PMA-2. (A) 80 degrees Celsius (B) 120 degrees (C) 165 degrees (D) 180 degrees.

Tab. S7 Reactions in **Fig. S13**

React.	Time (hour)	Temp. (°C)	POM (Mo)	Dy (g)	H_2O (mL)	OAM (mL)	OA (mL)
a	4	165	0.05	0.06	0.22	2.7	0.34
b	4	165	0.05	0.06	0.22	2.7	0.5
c	4	165	0.05	0.06	0.22	2.7	0.7
d	4	165	0.05	0.06	0.22	2.7	0.9

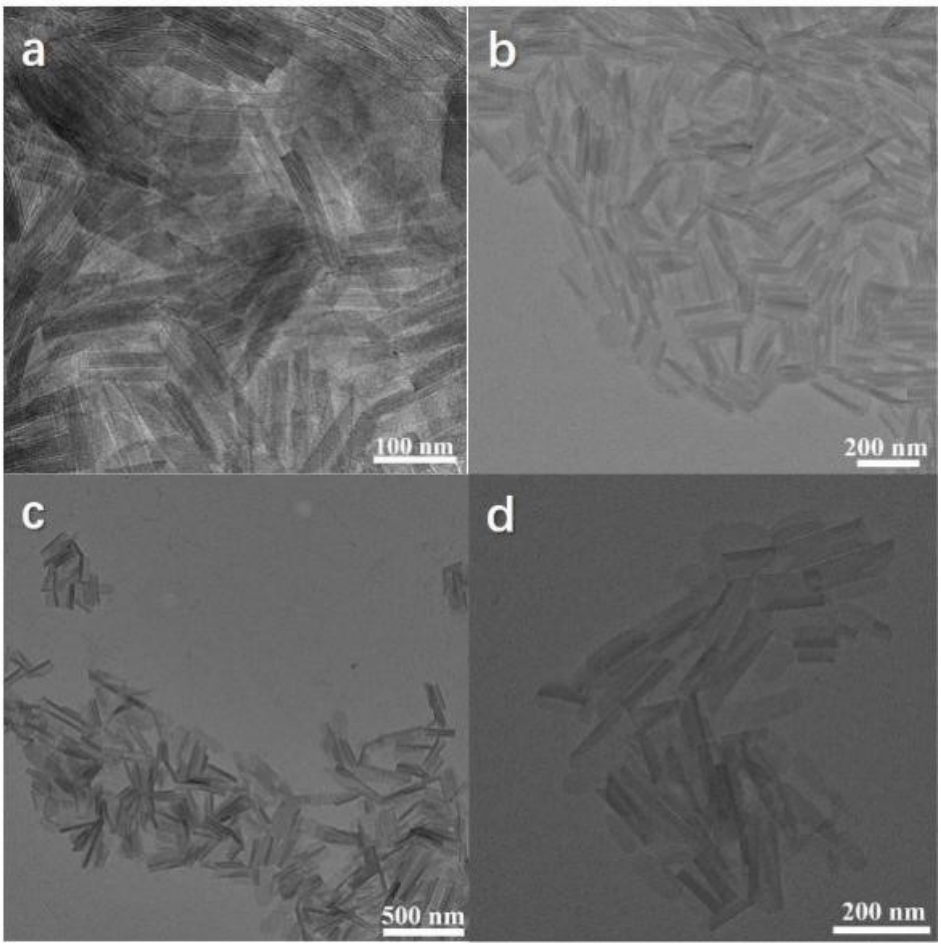

Fig. S13 Reactions at different concentrations of oleic acid Dy-PMA-2. (A) 0.34 mL (B) 0.5 mL (C) 0.7 mL (D) 1 mL.

Tab. S8 Reactions in **Fig. S14**

React.	Time (hour)	Temp. (°C)	POM (Mo)	Dy (g)	H_2O (mL)	OAM (mL)	OA (mL)
a	4	165	0.05	0.06	0	2.7	0.34
b	4	165	0.05	0.06	0.1	2.7	0.34
c	4	165	0.05	0.06	0.22	2.7	0.34
d	4	165	0.05	0.06	0.3	2.7	0.34

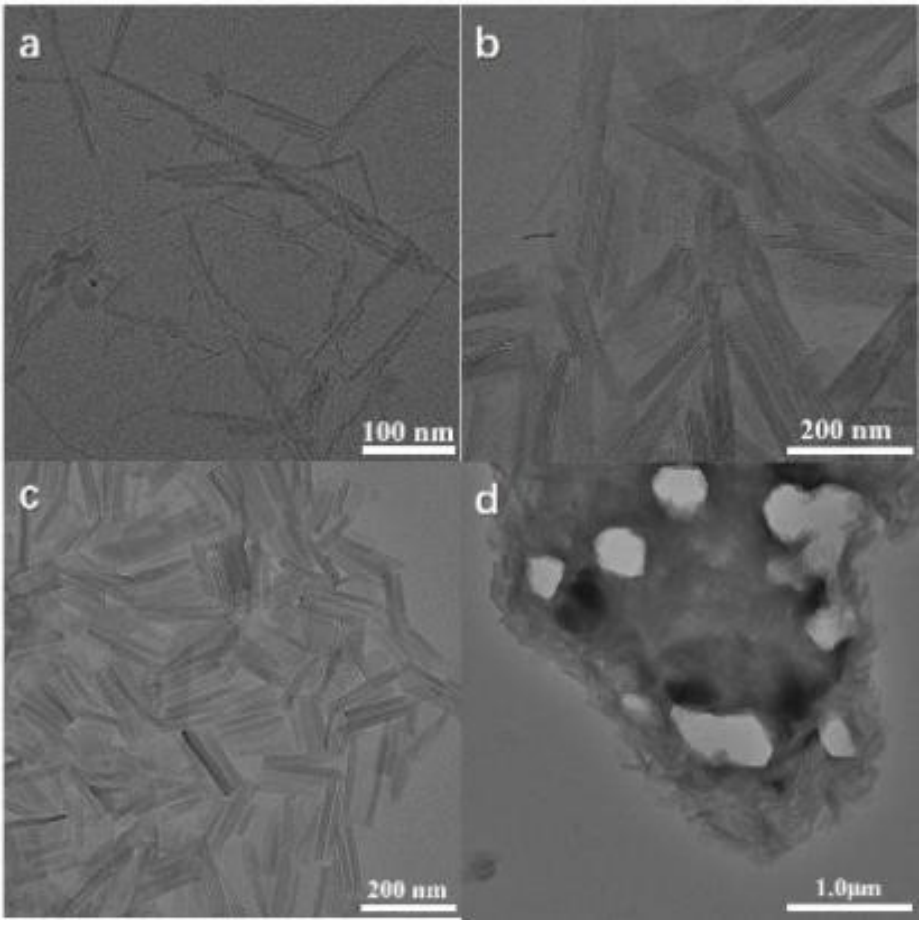

Fig. S14 Reactions at different concentrations of water Dy-PMA-2. (A) 0 mL (B) 0.1 mL(C) 0.22 mL (D) 0.3 mL.

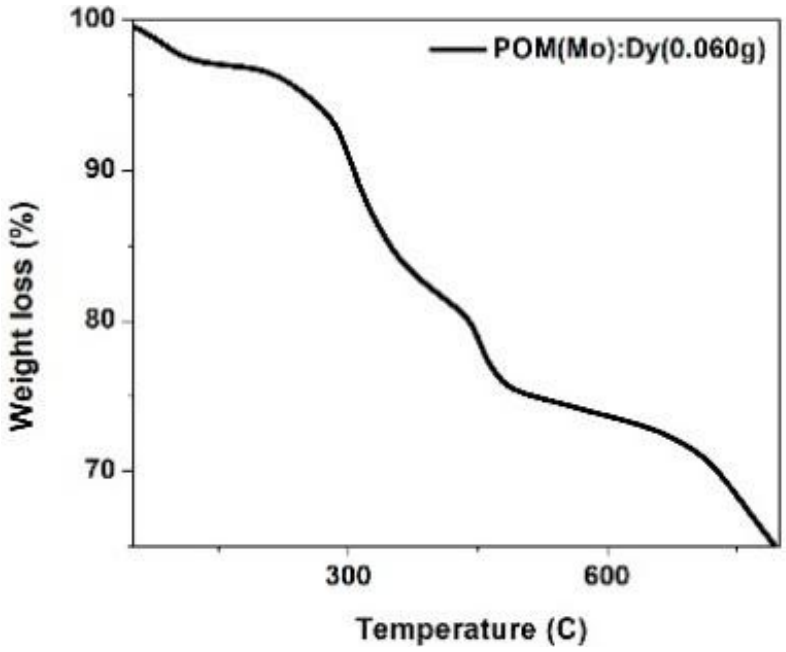

Fig. S15 Weight loss of 24% given from the decomposition of the organic components of oleylamine and oleic acid between 200-450 ˚C and one loss of inorganic components above 450 ˚C, with an initial loss of 3% till 100 ˚C of H_2O for a total loss of 27%. Like in **Fig. S5**.

Tab. S9 Reactions in **Fig. S16**

React. Dy-PMA-3	Time	Temp. (°C)	POM (Mo)	Dy (g)	H_2O (mL)	OAM (mL)	OA (mL)
a	6 h	165	0.05	0.06	0.22	2.7	0.34
b	0 min	165	0.05	0.06	0.22	2.7	0.34
c	1 min	165	0.05	0.06	0.22	2.7	0.34
d	5 min	165	0.05	0.06	0.22	2.7	0.34
e	30 min	165	0.05	0.06	0.22	2.7	0.34
f	1 h	165	0.05	0.06	0.22	2.7	0.34
g	12 h Oven	165	0.05	0.06	0.22	2.7	0.34

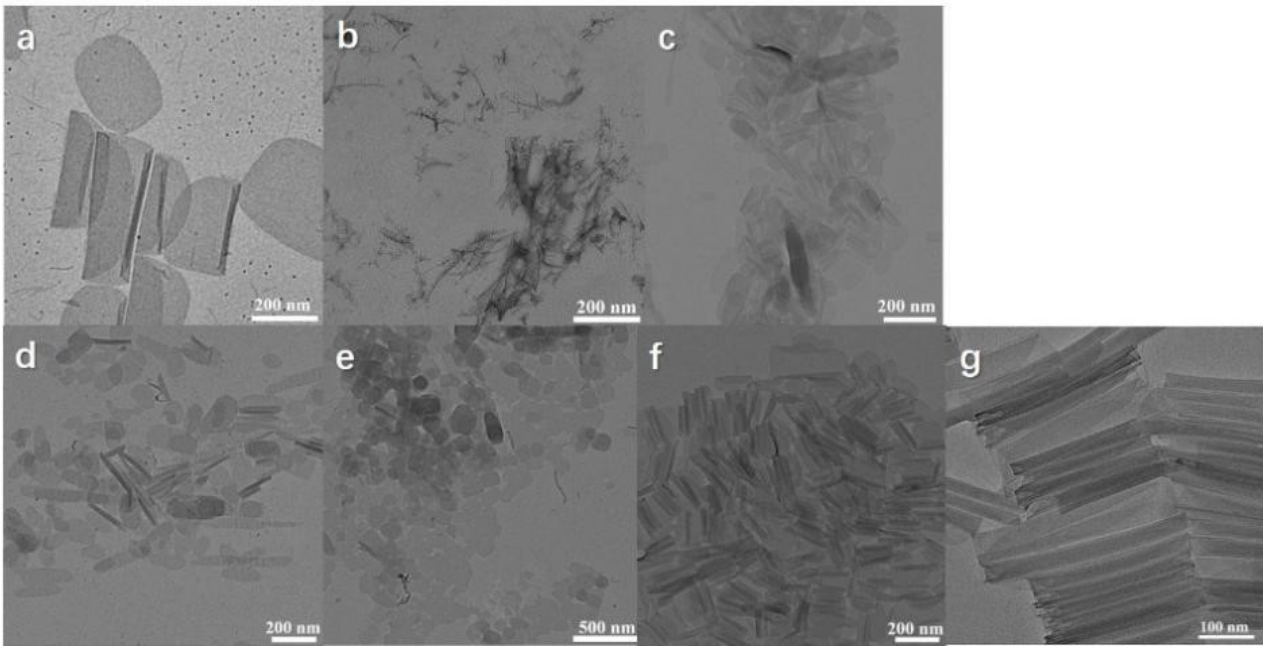

Fig. S16 Reactions at different reaction times Dy-PMA-3. (A) reaction studied at 6 h at 165 degrees centigrade; (B) reaction at zero time; (C) reaction time 1 min; (D) reaction time 5 min; (E) reaction time 30 min; (F) reaction time 1 h; (G) reaction time 12 h.

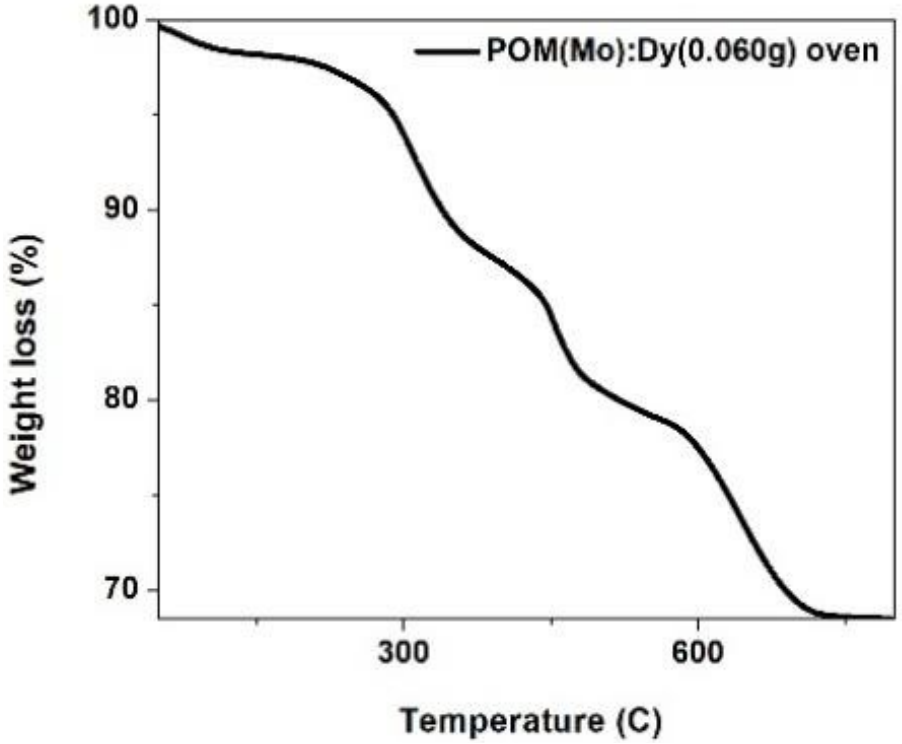

Fig. S17 Weight loss of 25% given from the decomposition of the organic components of oleylamine and oleic acid between 200-450 ˚C and one loss of inorganic components above 450 ˚C, with an initial loss of 2% till 100 ˚C of H2O for a total loss of 27%.

Tab. S10 Reactions in **Fig. S18**

React. Dy-PMA-4	Time	Temp. (°C)	POM (Mo)	Dy (g)	H_2O (mL)	OAM (mL)	n-Octyl. (mL)	Linol. Acid (mL)
a	2 h	165	0.05	0.06	0.22		2.7	0.75
b	2 h	165	0.05	0.06	0.22	2.7		0.75
c	5 min	165	0.05	0.06	0.22		2.7	0.75
d	0 h	165	0.05	0.06	0.22		2.7	0.75
e	6 h	165	0.05	0.06	0.22		2.7	0.75

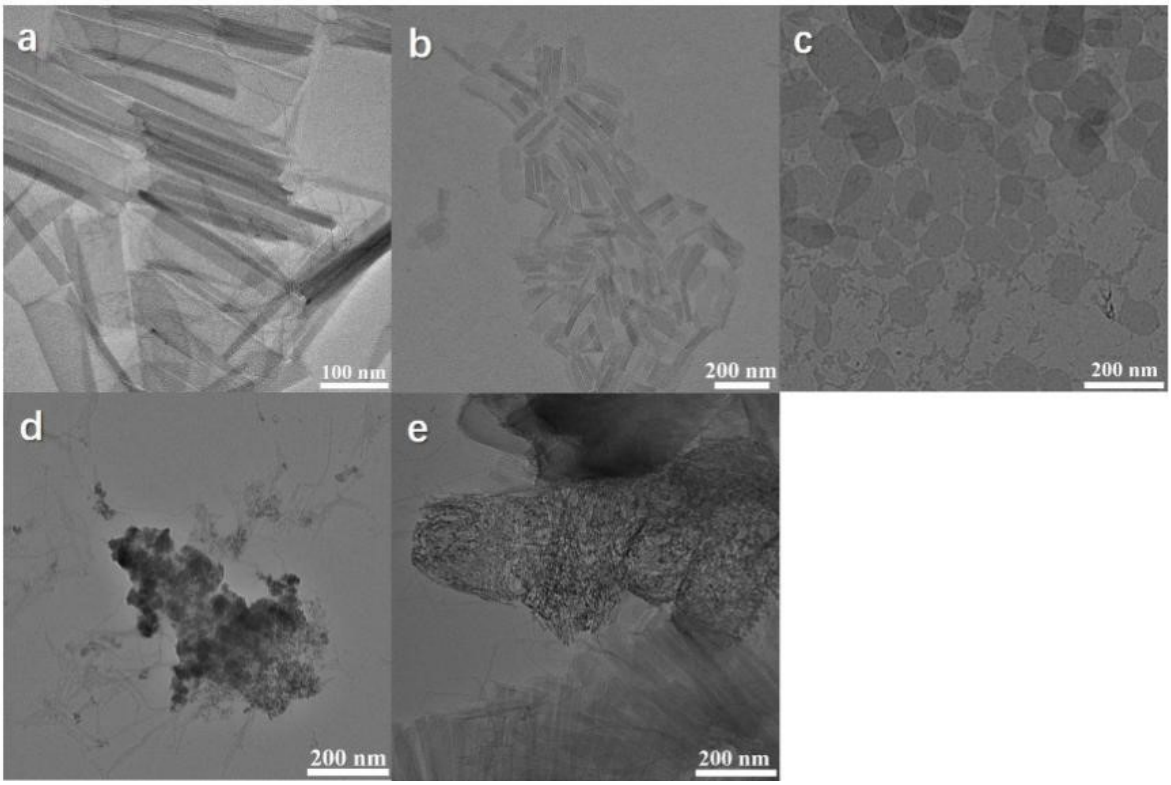

Fig. S18 Reactions at different reaction times Dy-PMA-4. (A) reaction studied at 2h at 165 ° C; (B) reaction at 2 h with oleylamine instead of n-octylamine; (C) reaction time 5 min; (D) reaction time 0 min; (E) reaction time 6 h.

Tab. S11 Reactions in **Fig. S19**

React. Dy-PMA-5	Time	Temp. (°C)	POM (W)	Dy (g)	H_2O (mL)	OAM (mL)	OA (mL)
a	2 h	165	0.03	0.06	0.22	2.7	0.9
b	0 h	165	0.03	0.06	0.22	2.7	0.9
c	30	165	0.03	0.06	0.22	2.7	0.9
d	1 min	165	0.03	0.06	0.22	2.7	0.9
e	5 min	165	0.03	0.06	0.22	2.7	0.9
f	30 min	165	0.03	0.06	0.22	2.7	0.9
g	1 h	165	0.03	0.06	0.22	2.7	0.9

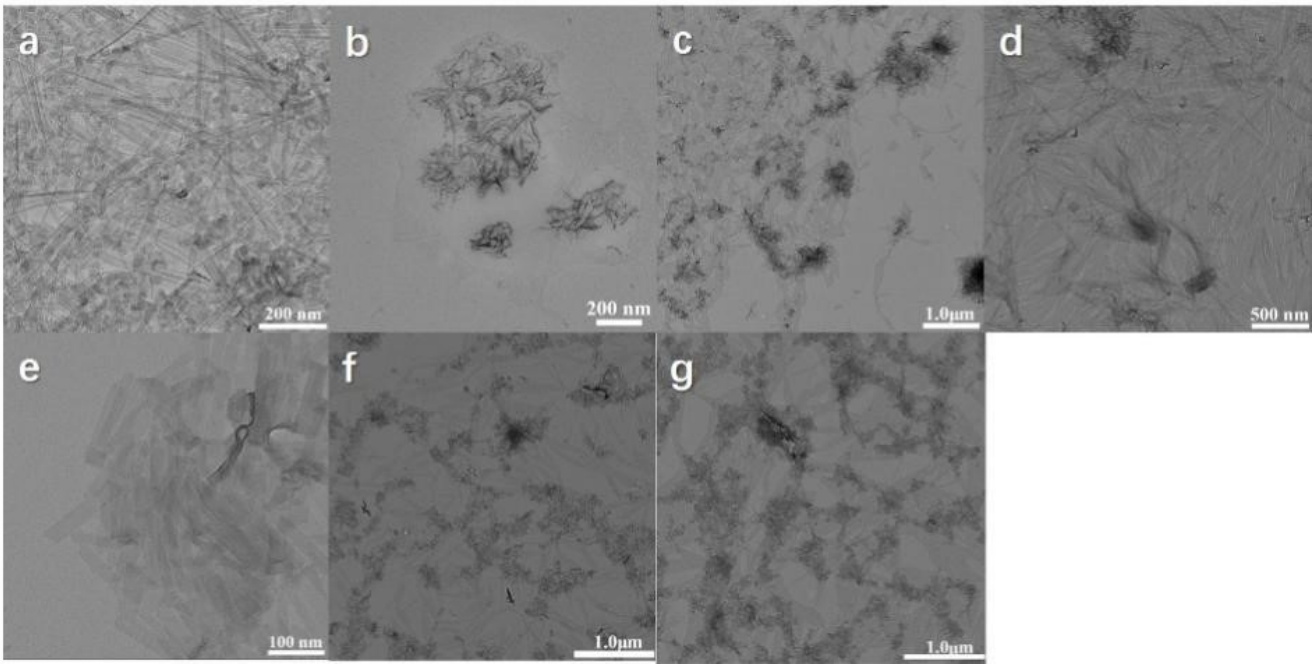

Fig. S19 Reactions at different reaction times Dy-PMA-5. (A) reaction studied at 2 h at 165 degrees centigrade; (B) reaction at zero-time; (C) reaction time 30 sec; (D) reaction time 1 min; (E) reaction time 5 min; (F) reaction time 30 min; (G) reaction time 1 h.

Tab. S12 Reactions in **Fig. S20**

React. Dy-PMA-6	Time	Temp. (°C)	POM (W)	Dy (g)	H_2O (mL)	OAM (mL)	OA (mL)
a	2h	165	0.03	0.06	0.22	2.7	0.7
b	0	165	0.03	0.06	0.22	2.7	0.7
c	1 min	165	0.03	0.06	0.22	2.7	0.7
d	5 min	165	0.03	0.06	0.22	2.7	0.7
e	4h	165	0.03	0.06	0.22	2.7	0.7
f	6h	165	0.03	0.06	0.22	2.7	0.7

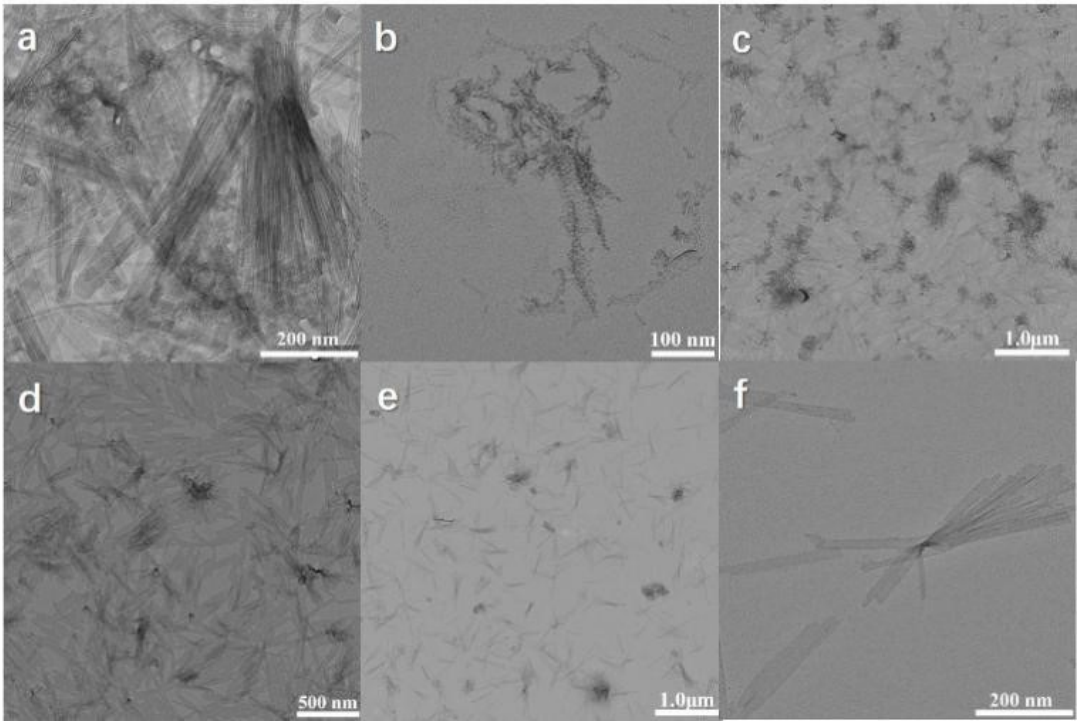

Fig. S20 Reactions at different reaction times Dy-PMA-6. (A) reaction studied at 2h at 165 degrees centigrade; (B) reaction at zero-time; (C) reaction time 1 min; (D) reaction time 5 min; (E) reaction time 4 h; (F) reaction time 6 h.

Thermal stability at 130°C of the constructed samples.

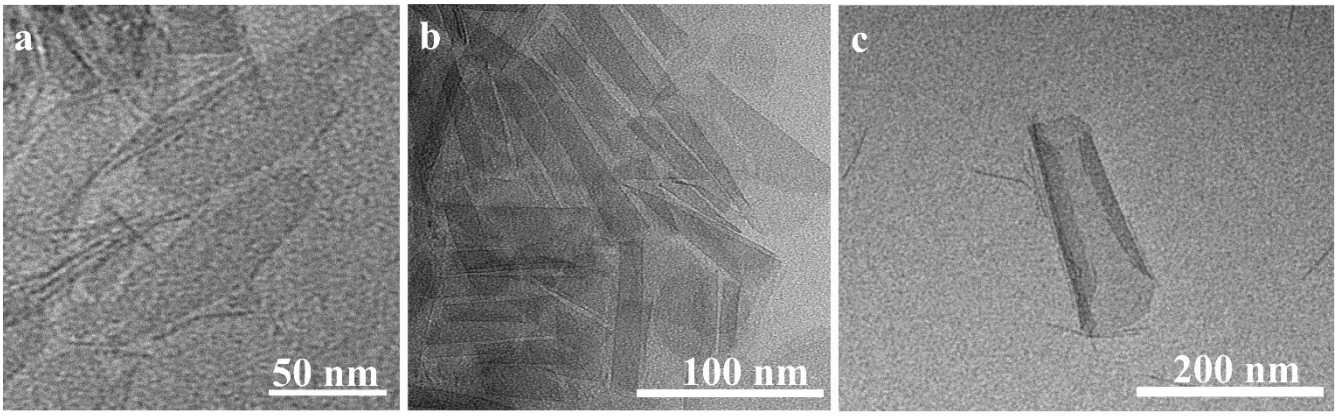

Fig. S21 Thermal stability at 130°C of: a) Dy_2O_3-PMA-1; b) Dy_2O_3-PMA-2; c) Dy_2O_3-PMA-3

Other metal oxides for the construction of monolayer assemblies.

Different metals are being used in this system, like Gd trichloride hexahydrate, Ho trichloride hexahydrate, Co(II)acetate tetrahydrate, Fe nitrate nonahydrate, and Li chloride monohydrate.

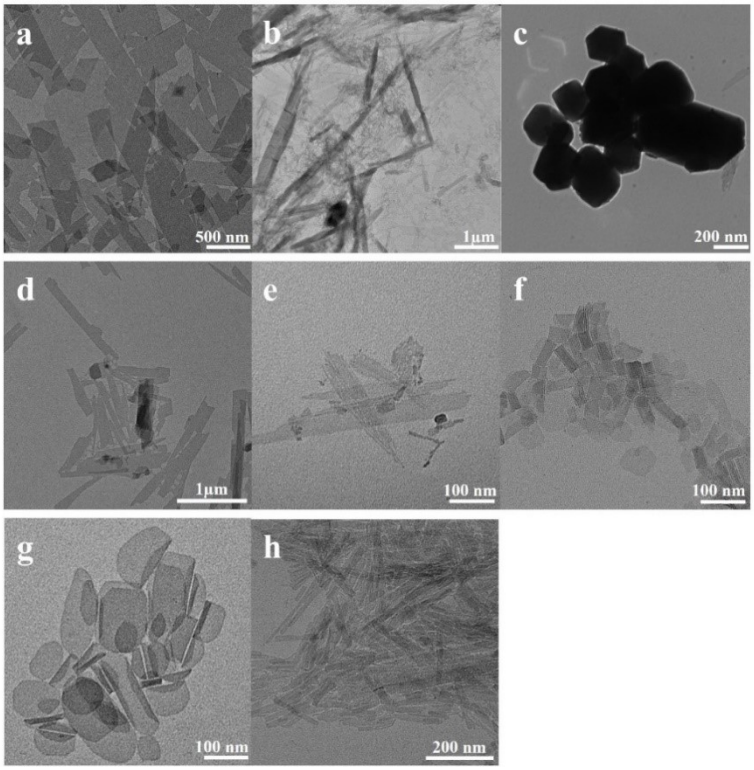

Fig. S22 a) Co-PMA similar to Dy_2O_3-PMA-2 at 30 min, b) Fe-PMA similar to Dy_2O_3-PMA-2 at 30 min, c) Li-PMA similar to Dy_2O_3-PMA-2 at 30 min, d) Co-PMA similar to Dy_2O_3-PMA-2 at 30 min, e) Li-PMA similar to Dy_2O_3-PMA-2 at 30 min, f) Gd-PMA similar to Dy_2O_3-PMA-2 at 1h, h) Ho-PMA similar to Dy_2O_3-PMA-1 at 2 h, g) Ho-PMA similar to Dy_2O_3-PMA-2 at 1.30 h.

6. Theory backbone for the microwave

In recent years the synthesis of nanostructures in the microwave has become one important challenge. This is because, with the use of the microwave, the time-consuming of trial and error is reduced. A new frontier of 2D nanostructures: nanotubes, nanosheets, films, and coats, [32], [33], [34], [35], [36], [37] has become an interesting challenge, easy to obtain in the oven, and harder to obtain in the microwave. This new kind of technique takes from the 1D structure [38] to the 2D structure [39], [40]. These structures in some cases can also be re-assembled for furnished 3D structures [41], [42].

Temperature and pressure inside the vial, are taken under control by the microwave, this ensures no safety issues. The range of the microwave goes between 0.3 and 300 GHz, which corresponds to a wavelength between 1mm and 1m. The normal microwave oven at home, like the Biotage initiator microwave in our lab, has a frequency of 2.45 GHz, with a wavelength of 12.25 cm, because the major part of organic molecules oscillates at this frequency. Microwave dielectric heating consists of the ability of a solvent or a reagent, to absorb microwave energy and convert it into heat. [43], [44] This heating affects only molecular rotation, based on the polarization or the ionic conduction of the molecule. Electromagnetic radiation produces one oscillating field, where ions and dipoles try to realign according to the electric field, producing molecular friction and dielectric loss [32], given by the absorbance of these microwaves. Indeed, high-loss factors solvent is microwave transparent. If the alignment to the electric field is not complete, because the time is too less or too long between one impulse and another, no heating is generated [32], [43], [45], when the heating is generated is possible to talk of dielectric loss. [32], [33]

Dielectric loss tangent is: $\tan\delta = \frac{\varepsilon''}{\varepsilon'}$, ε' is the polarization from the electric field, named the dielectric constant. ε'' is the conversion of electromagnetic radiation into heat, named dielectric loss. High dielectric constant molecule (for example water) are medium absorber and their absorbance decrease with the increase in temperature. Penetration depth is considered the point at which is conserved 37% of the initial irradiation. [46] High-loss tangents have short penetration depth, for this, only the outer layer is efficiently heated. [32] The thermal effect accelerates the heating and the rate of the reaction mixture, but this rate can be accelerating also from vessel size, the volume of precursors, and microwave cavity design. Electromagnetic field distribution in the microwave cavity influences the morphology and yield of the crystals.[47] Indeed, in a multimode, the rate of nucleation and crystallization is taller than in a single-mode oven (uniform field). [32] Our solution can reach 165 ˚C in a few seconds, this can't happen with traditional heating. Conventional heating depends on convection currents of the materials or the substances that should be penetrated, and the temperature of the reaction is lower than vessel one. Indeed, microwave irradiation produces internal heating and increases homogeneously the temperature inside the sample. [32]

The “molecular radiation” is given from the direct coupling of microwave energy to the specific reagent (polar species in microwave transparent medium) in a homogeneous solution, with the elimination of the wall effect caused by inverted temperature gradients. [32], [38], [48] In microwave, boiling points are 10 ˚-20 ˚C superior to the same condition in conventional heating. If one reaction is homogeneous because well stirred, it is possible to see: a lower boiling point, lower pressure [49]**,** and better selectivity. Indeed, become easy to reproduce reactions and redact side reactions. In our case, we have set the absorption to a normal level, also if the water present in our reaction required a low absorption level. This happens because in the reaction are present organic reagents that usually have a normal level of absorption. The different absorbances of different dielectric reagents, affect nucleation and crystallization rates [32], [50]. When there is a non-polar reagent, is added to react with a polar reagent or a salt. Small reaction sizes (max 100 L) [51] and a large amount of energy are used from the microwave. A competitive microwave synthesis should give particular advantages concerning the oven one. According to Panda et al. the selective absorption of organic surfactants, causes crystal growth to be inhibited in all directions but is favored crystallographically only on one plane, thus allowing to reach 1D structures more easily, and then for self-organization process to 2D. [52] In our work, we will focus on nanometric systems 2D, in particular systems containing dysprosium oxide (Dy_2O_3) with Phosphomolibdic acid hydrate (PMA), synthesized inside the microwave. It will be demonstrated how the interaction of certain metals with polyoxometalates, in the presence of other reagents, can give rise to the formation of sub-1 nm nanosheets (SNSs) [36], nanotubes (NTs) [53], and nanobelts (NBs) [54]. Nanosheets are important because they show useful properties in lithium or ionic batteries[45], solar cells [55], etc. [56].

7. Supplementary References

[1] S. J. Clark *et al.*, “First principles methods using CASTEP,” *Z Kristallogr Cryst Mater*, vol. 220, no. 5–6, pp. 567–570, May 2005, doi: 10.1524/zkri.220.5.567.65075.

[2] P. Hohenberg and W. Kohn, “Inhomogeneous Electron Gas,” *Physical Review*, vol. 136, no. 3B, pp. B864–B871, Nov. 1964, doi: 10.1103/PhysRev.136.B864.

[3] J. P. Perdew *et al.*, “Restoring the Density-Gradient Expansion for Exchange in Solids and Surfaces,” *Phys Rev Lett*, vol. 100, no. 13, p. 136406, Apr. 2008, doi: 10.1103/PhysRevLett.100.136406.

[4] H.-X. Liu, “Crystal structure of tri(2-acetylpyrazinium) dodecatungstophosphate, [C6H8N2O]3[PW12O40],” *Zeitschrift für Kristallographie - New Crystal Structures*, vol. 225, no. 2, pp. 243–244, Jun. 2010, doi: 10.1524/ncrs.2010.0105.

[5] J. Liu, N. Liu, H. Wang, W. Shi, J. Zhuang, and X. Wang, “Hybrid MoO_3 –Polyoxometallate Sub-1 nm Nanobelt Superstructures,” *J Am Chem Soc*, vol. 142, no. 41, pp. 17557–17563, Oct. 2020, doi: 10.1021/jacs.0c07375.

[6] R. Picciochi, J. N. Canongia Lopes, H. P. Diogo, and M. E. Minas da Piedade, “Experimental and Molecular Dynamics Simulation Study of the Sublimation Energetics of Cyclopentadienyltricarbonylmanganese (Cymantrene),” *J Phys Chem A*, vol. 112, no. 41, pp. 10429–10434, Oct. 2008, doi: 10.1021/jp805607d.

[7] A. K. Rappe, C. J. Casewit, K. S. Colwell, W. A. Goddard, and W. M. Skiff, “UFF, a full periodic table force field for molecular mechanics and molecular dynamics simulations,” *J Am Chem Soc*, vol. 114, no. 25, pp. 10024–10035, Dec. 1992, doi: 10.1021/ja00051a040.

[8] W. F. Van Gusteren, “Biomolecular Simulation: The GROMOS96 manual and user guide,” *Switzerland: Hochschulverlag AG an der ETH Z¨urich*. Zurich, 1996.

[9] B. Hess, C. Kutzner, D. van der Spoel, and E. Lindahl, “GROMACS 4: Algorithms for Highly Efficient, Load-Balanced, and Scalable Molecular Simulation,” *J Chem Theory Comput*, vol. 4, no. 3, pp. 435–447, Mar. 2008, doi: 10.1021/ct700301q.

[10] D. Van Der Spoel, E. Lindahl, B. Hess, G. Groenhof, A. E. Mark, and H. J. C. Berendsen, “GROMACS: Fast, flexible, and free,” *J Comput Chem*, vol. 26, no. 16, pp. 1701–1718, Dec. 2005, doi: 10.1002/jcc.20291.

[11] E. Lindahl, B. Hess, and D. van der Spoel, “GROMACS 3.0: a package for molecular simulation and trajectory analysis,” *J Mol Model*, vol. 7, no. 8, pp. 306–317, Aug. 2001, doi: 10.1007/s008940100045.

[12] C. Oostenbrink, A. Villa, A. E. Mark, and W. F. Van Gunsteren, “A biomolecular force field based on the free enthalpy of hydration and solvation: The GROMOS force-field parameter sets 53A5 and 53A6,” *J Comput Chem*, vol. 25, no. 13, pp. 1656–1676, Oct. 2004, doi: 10.1002/jcc.20090.

[13] H. J. C. Berendsen, J. P. M. Postma, W. F. van Gunsteren, A. DiNola, and J. R. Haak, “Molecular dynamics

with coupling to an external bath," *J Chem Phys*, vol. 81, no. 8, pp. 3684–3690, Oct. 1984, doi: 10.1063/1.448118.

[14] G. Bussi, D. Donadio, and M. Parrinello, "Canonical sampling through velocity rescaling," *J Chem Phys*, vol. 126, no. 1, Jan. 2007, doi: 10.1063/1.2408420.

[15] W. Humphrey, A. Dalke, and K. Schulten, "VMD: Visual molecular dynamics," *J Mol Graph*, vol. 14, no. 1, pp. 33–38, Feb. 1996, doi: 10.1016/0263-7855(96)00018-5.

[16] G. Kresse and J. Furthmüller, "Efficiency of ab-initio total energy calculations for metals and semiconductors using a plane-wave basis set," *Comput Mater Sci*, vol. 6, no. 1, pp. 15–50, Jul. 1996, doi: 10.1016/0927-0256(96)00008-0.

[17] G. Kresse and J. Furthmüller, "Efficient iterative schemes for *ab initio* total-energy calculations using a plane-wave basis set," *Phys Rev B*, vol. 54, no. 16, pp. 11169–11186, Oct. 1996, doi: 10.1103/PhysRevB.54.11169.

[18] J. P. Perdew, K. Burke, and M. Ernzerhof, "Generalized Gradient Approximation Made Simple," *Phys Rev Lett*, vol. 77, no. 18, pp. 3865–3868, Oct. 1996, doi: 10.1103/PhysRevLett.77.3865.

[19] P. E. Blöchl, "Projector augmented-wave method," *Phys Rev B*, vol. 50, no. 24, pp. 17953–17979, Dec. 1994, doi: 10.1103/PhysRevB.50.17953.

[20] G. Kresse and D. Joubert, "From ultrasoft pseudopotentials to the projector augmented-wave method," *Phys Rev B*, vol. 59, no. 3, pp. 1758–1775, Jan. 1999, doi: 10.1103/PhysRevB.59.1758.

[21] O. Bengone, M. Alouani, P. Blöchl, and J. Hugel, "Implementation of the projector augmented-wave LDA+U method: Application to the electronic structure of NiO," *Phys Rev B*, vol. 62, no. 24, pp. 16392–16401, Dec. 2000, doi: 10.1103/PhysRevB.62.16392.

[22] L. Zhang, Y.-Q. Su, M.-W. Chang, I. A. W. Filot, and E. J. M. Hensen, "Linear Activation Energy-Reaction Energy Relations for $LaBO_3$ (B = Mn, Fe, Co, Ni) Supported Single-Atom Platinum Group Metal Catalysts for CO Oxidation," *The Journal of Physical Chemistry C*, vol. 123, no. 51, pp. 31130–31141, Dec. 2019, doi: 10.1021/acs.jpcc.9b11079.

[23] H. Yoshida *et al.*, "A Thermally Stable Cr–Cu Nanostructure Embedded in the CeO_2 Surface as a Substitute for Platinum-Group Metal Catalysts," *ACS Catal*, vol. 5, no. 11, pp. 6738–6747, Nov. 2015, doi: 10.1021/acscatal.5b01847.

[24] J. Liu, W. Shi, S. Nie, and X. Wang, "Functionally Guided Precise Synthesis of Manganous Oxide-Polyoxometalate 2D Hybrid Sub-1 nm Nanosheet Superstructures," *Small Struct*, vol. 3, no. 7, Jul. 2022, doi: 10.1002/sstr.202200039.

[25] X. Cheng, S. Zhang, and X. Wang, "Cluster–Nuclei Coassembled One-Dimensional Subnanometer Heteronanostructures," *Nano Lett*, vol. 21, no. 23, pp. 9845–9852, Dec. 2021, doi: 10.1021/acs.nanolett.1c03936.

[26] J. Liu *et al.*, "Incorporation of clusters within inorganic materials through their addition during nucleation

steps," *Nat Chem*, vol. 11, no. 9, pp. 839–845, Sep. 2019, doi: 10.1038/s41557-019-0303-0.

[27] S. Zhang, N. Liu, H. Wang, Q. Lu, W. Shi, and X. Wang, "Sub-Nanometer Nanobelts Based on Titanium Dioxide/Zirconium Dioxide–Polyoxometalate Heterostructures," *Advanced Materials*, vol. 33, no. 23, Jun. 2021, doi: 10.1002/adma.202100576.

[28] J. Liu *et al.*, "Polyoxometalate Cluster-Incorporated High Entropy Oxide Sub-1 nm Nanowires," *J Am Chem Soc*, vol. 144, no. 50, pp. 23191–23197, Dec. 2022, doi: 10.1021/jacs.2c10602.

[29] J. Liu *et al.*, "Au-Polyoxometalates A-B-A-B Type Copolymer-Analogue Sub-1 nm Nanowires," *Small*, vol. 17, no. 4, Jan. 2021, doi: 10.1002/smll.202006260.

[30] J. Liu, W. Shi, S. Nie, and X. Wang, "Functionally Guided Precise Synthesis of Manganous Oxide-Polyoxometalate 2D Hybrid Sub-1 nm Nanosheet Superstructures," *Small Struct*, vol. 3, no. 7, Jul. 2022, doi: 10.1002/sstr.202200039.

[31] X. Zhang, K. Khan, A. K. Tareen, and Y. Zhang, "Application of 2D Polyoxometalate Clusterphene in a High-Performance Photoelectrochemical Photodetector," *Adv Opt Mater*, vol. 11, no. 20, Oct. 2023, doi: 10.1002/adom.202300646.

[32] I. Bilecka and M. Niederberger, "Microwave chemistry for inorganic nanomaterials synthesis," *Nanoscale*, vol. 2, no. 8, p. 1358, 2010, doi: 10.1039/b9nr00377k.

[33] B. L. Hayes, "Microwave synthesis: Chemistry at the speed of light," *CEM Publishing*. 2002.

[34] R. Gedye *et al.*, "The use of microwave ovens for rapid organic synthesis," *Tetrahedron Lett*, vol. 27, no. 3, pp. 279–282, Jan. 1986, doi: 10.1016/S0040-4039(00)83996-9.

[35] R. J. Giguere, T. L. Bray, S. M. Duncan, and G. Majetich, "Application of commercial microwave ovens to organic synthesis.," *Tetrahedron Lett*, vol. 27, no. 41, pp. 4945–4948, Jan. 1986, doi: 10.1016/S0040-4039(00)85103-5.

[36] M.-H. Kang, D. Lee, J. Sung, J. Kim, B. H. Kim, and J. Park, "Structure and Chemistry of 2D Materials," in *Comprehensive Nanoscience and Nanotechnology*, Elsevier, 2019, pp. 55–90. doi: 10.1016/B978-0-12-803581-8.10507-7.

[37] Y. Feng, H. Wang, and J. Yao, "Synthesis of 2D nanoporous zeolitic imidazolate framework nanosheets for diverse applications," *Coord Chem Rev*, vol. 431, p. 213677, Mar. 2021, doi: 10.1016/j.ccr.2020.213677.

[38] L. Chen, B. Su, and L. Jiang, "Recent advances in one-dimensional assembly of nanoparticles," *Chem Soc Rev*, vol. 48, no. 1, pp. 8–21, 2019, doi: 10.1039/C8CS00703A.

[39] M.-H. Kang, D. Lee, J. Sung, J. Kim, B. H. Kim, and J. Park, "Structure and Chemistry of 2D Materials," in *Comprehensive Nanoscience and Nanotechnology*, Elsevier, 2019, pp. 55–90. doi: 10.1016/B978-0-12-803581-8.10507-7.

[40] Y. Feng, H. Wang, and J. Yao, "Synthesis of 2D nanoporous zeolitic imidazolate framework nanosheets for diverse applications," *Coord Chem Rev*, vol. 431, p. 213677, Mar. 2021, doi: 10.1016/j.ccr.2020.213677.

[41] B. H. Kim, J. Heo, and J. Park, “Determination of the 3D Atomic Structures of Nanoparticles,” *Small Science*, vol. 1, no. 1, Jan. 2021, doi: 10.1002/smsc.202000045.

[42] R. K. Joshi and J. J. Schneider, “Assembly of one dimensional inorganic nanostructures into functional 2D and 3D architectures. Synthesis, arrangement and functionality,” *Chem Soc Rev*, vol. 41, no. 15, p. 5285, 2012, doi: 10.1039/c2cs35089k.

[43] C. O. Kappe, “Controlled Microwave Heating in Modern Organic Synthesis,” *Angewandte Chemie International Edition*, vol. 43, no. 46, pp. 6250–6284, Nov. 2004, doi: 10.1002/anie.200400655.

[44] A. de la Hoz and A. Loupy, Eds., *Microwaves in Organic Synthesis*. Wiley, 2012. doi: 10.1002/9783527651313.

[45] C. Gabriel, S. Gabriel, E. H. Grant, E. H. Grant, B. S. J. Halstead, and D. Michael P. Mingos, “Dielectric parameters relevant to microwave dielectric heating,” *Chem Soc Rev*, vol. 27, no. 3, p. 213, 1998, doi: 10.1039/a827213z.

[46] M. Nüchter, B. Ondruschka, W. Bonrath, and A. Gum, “Microwave assisted synthesis – a critical technology overview,” *Green Chem.*, vol. 6, no. 3, pp. 128–141, 2004, doi: 10.1039/B310502D.

[47] Wm. C. Conner, G. Tompsett, K.-H. Lee, and K. S. Yngvesson, “Microwave Synthesis of Zeolites: 1. Reactor Engineering,” *J Phys Chem B*, vol. 108, no. 37, pp. 13913–13920, Sep. 2004, doi: 10.1021/jp037358c.

[48] A. de la Hoz, Á. Díaz-Ortiz, and A. Moreno, “Microwaves in organic synthesis. Thermal and non-thermal microwave effects,” *Chem. Soc. Rev.*, vol. 34, no. 2, pp. 164–178, 2005, doi: 10.1039/B411438H.

[49] L. Perreux and A. Loupy, “A tentative rationalization of microwave effects in organic synthesis according to the reaction medium, and mechanistic considerations,” *Tetrahedron*, vol. 57, pp. 9199–9223, 2001.

[50] B. Panzarella, G. A. Tompsett, K. S. Yngvesson, and W. C. Conner, “Microwave Synthesis of Zeolites. 2. Effect of Vessel Size, Precursor Volume, and Irradiation Method,” *J Phys Chem B*, vol. 111, no. 44, pp. 12657–12667, Nov. 2007, doi: 10.1021/jp072622d.

[51] B. Ondruschka and W. Bonrath, “Microwave-Assisted Chemistry – A Stock Taking,” *Chimia (Aarau)*, vol. 60, no. 6, p. 326, Jun. 2006, doi: 10.2533/000942906777836246.

[52] A. B. Panda, G. Glaspell, and M. S. El-Shall, “Microwave Synthesis and Optical Properties of Uniform Nanorods and Nanoplates of Rare Earth Oxides,” *The Journal of Physical Chemistry C*, vol. 111, no. 5, pp. 1861–1864, Feb. 2007, doi: 10.1021/jp0670283.

[53] A.-W. Xu, Y.-P. Fang, L.-P. You, and H.-Q. Liu, “A Simple Method to Synthesize $Dy(OH)_3$ and Dy_2O_3 Nanotubes,” *J Am Chem Soc*, vol. 125, no. 6, pp. 1494–1495, Feb. 2003, doi: 10.1021/ja029181q.

[54] M. Han *et al.*, “Large-Scale Synthesis of Single-Crystalline RE_2O_3 (RE=Y, Dy, Ho, Er) Nanobelts by a Solid–Liquid-Phase Chemical Route,” *Chemistry – A European Journal*, vol. 14, no. 5, pp. 1615–1620, Feb. 2008, doi: 10.1002/chem.200700808.

[55] F. Bai, Y. Hu, Y. Hu, T. Qiu, X. Miao, and S. Zhang, “Lead-free, air-stable ultrathin Cs3Bi2I9 perovskite nanosheets for solar cells,” *Solar Energy Materials and Solar Cells*, vol. 184, pp. 15–21, Sep. 2018, doi: 10.1016/j.solmat.2018.04.032.

[56] J. Liu, W. Shi, and X. Wang, “Cluster–Nuclei Coassembled into Two-Dimensional Hybrid CuO-PMA Sub-1 nm Nanosheets,” *J Am Chem Soc*, vol. 141, no. 47, pp. 18754–18758, Nov. 2019, doi: 10.1021/jacs.9b08818.